Materials Advances

ROYAL SOCIETY OF CHEMISTRY

PAPER

View Article Online
View Journal

Cite this: DOI: 10.1039/d5ma01332a

Dual-phyto mediated synthesis of magnesium zinc ferrite nanoparticles using *Parthenium hysterophorus* and *Nerium oleander*: a novel strategy for eco-friendly wastewater detoxification

Ghulam Mustafa,*[a] Sadia Muzammal,[b] Awais Ahmad,*[a] Faisal Ali[a] and Ikram Ahmad*[c]

Water contamination due to municipal, agricultural, and industrial discharge is a constant environmental issue, and dye-contaminated effluents from the textile industry are a particularly recalcitrant and toxic contaminant. This investigation reports the green synthesis of Mg/Zn ferrites using extracts of *Parthenium hysterophorus* (P-H) and *Nerium oleander* (N-O) as reducing and stabilizing agents, and thus produces P-H/$MgZnFe_2O_4$ and N-O/$MgZnFe_2O_4$ nanostructures. A batch adsorption experiment has been planned to determine the effect of pH, dosage of adsorbent, contact time, temperature, and initial concentration of dyes on removal efficiency. The adsorption kinetics followed pseudo-second order and intraparticle diffusion models, indicating chemisorption and diffusion-controlled mechanisms; equilibrium data were well described by the Langmuir, Freundlich, Temkin, and Harkins–Jura isotherms, suggesting a multilayer mechanism and heterogeneous adsorption; thermodynamic analysis showed negative values of Gibbs free energy and endothermic behaviour, which confirms the spontaneity and feasibility of the adsorption process. The presence of detergents and surfactants, ubiquitous in textile wastewater, was also found to modulate dye-adsorbent interactions. Mg-doped $ZnFe_2O_4$ NPs, green-synthesized by P-H and N-O extracts, were tested for wastewater treatment. The synthesized nanocomposites had the highest adsorption capacity of approximately 42 mg g^{-1} at pH 2 and had a removal efficiency greater than 90% in 80 minutes. P-H/Mg–$ZnFe_2O_4$ was the best adsorbent studied, demonstrating its ability to be a sustainable wastewater treatment system.

Received 15th November 2025,
Accepted 30th January 2026

DOI: 10.1039/d5ma01332a

rsc.li/materials-advances

1. Introduction

Water is one of the basic components or units of the continued development of both industrialized and emerging nations. Clean water is becoming increasingly necessary as a result of the rapid rate of population increase and industrial activity. Toxins released from the industrial, municipal, and agricultural sectors contaminate supplies of pure water. Due to the dye pollutants' extreme harm to living things, dye-bearing effluents released by the textile sector constitute a big problem.[1,2] Due to the dyes' teratogenic, mutagenic, and carcinogenic characteristics, exposure to them can result in serious illnesses or disorders in people. Given the growing focus on developing green technologies, it is necessary to design adsorbents that are less expensive and more effective for treating.[3–5]

Petrochemical compounds are the source of the bulk of synthetic colors that can be purchased. They are capable of a wide range of things, such as coloration, in a wide variety of different environmental conditions, and with cost-effective energy consumption.[6] Water is used extensively during the various steps. As a result, a sizable portion of improper discharge is consistently refused. Organic and inorganic contaminants are very prevalent in dye effluents.[7,8] Nowadays, several contaminants and their derivatives are released into aquatic ecosystems owing to metropolises and industrial growth. Organics, nutrients, and toxins at low concentrations are extremely harmful to aquatic life. Different liquid or gas molecules, ions, and atoms bind to surfaces through the process of adsorption. A thin coating of adsorbate is deposited and percolates into the latter.[9]

[a] *Department of Chemistry University of Lahore, Lahore, Pakistan. E-mail: ghulam.mustafa@chem.uol.edu.pk*
[b] *Department of Environmental Science, Government College University, Faisalabad, Pakistan*
[c] *Department of Chemistry, University of Sahiwal, Pakistan. E-mail: drikramahmad@uosahiwal.edu.pk*

This process only works on surfaces, whereas absorption affects the entire substance. However, ''sorption,'' which is the opposite of ''desorption,'' is a phrase that encompasses both meanings and is a more effective technique for treating wastewater.[10,11] Green strategies for synthesis have gained prominence among researchers because they synthesize NPs in a less life-threatening way. Physicochemical approaches are currently less used in the manufacturing sectors, in contrast to green synthetic procedures. Green synthesis procedures, which are innocuous for the planet, non-toxic, more stable, and enable a multitude of prospects for the nanoscale fabrication of this material, have successfully generated nanoparticles (NPs).[12,13] As a result, scientists have been creating several techniques to improve the production of NPs utilizing environmentally friendly technologies. To produce ferrites, new and environmentally friendly methods classified as ''Green nanotechnology'' have recently been created.[14,15] *Parthenium hysterophorus* (P-H) is an annual or fugacious plant that destroys natural ecosystems, gets into disturbed locations, and can cause major hypersensitivity reactions in humans and animals.[16,17] *Nerium oleander* (N-O), because of its numerous harmful components, has long been regarded as a poisonous plant. However, due to its bitterness, it is unappealing to both people and most animals, making poisoning incidents extremely uncommon and lowering the overall risk of human fatality.[18–20]

This study includes the green synthesis of $MgZnFe_2O_4$ and $MgZnFe_2O_4$ ferrites using P-H and N-O plant extracts as reducing agents. The green synthesis of $ZnFe_2O_4$ NPs was chosen on the basis of green synthesis using P-H and N-O because of the abundance of phytochemical components, their broad availability, and their demonstrated reducing and stabilizing capability in biology. It is a fact that both plants have high levels of polyphenols, flavonoids, alkaloids, and other oxygen and nitrogen functional groups, which are dual front-runners in the green synthesis process as they not only reduce the metal ions, but also ensure the stability of the formed NPs without the use of toxic chemical reagents. $ZnFe_2O_4$ NPs that are produced with the help of the plant extracts mentioned are characterized by better surface functionality and were also found to have better magnetism, all of great benefit to the wastewater treatment process. The surface functional groups generated by the breakdown of phytochemicals enhance the adsorption capacity of dyes, heavy metals, and organic pollutants, and the magnetic attribute of $ZnFe_2O_4$ enables simple recovery and reuse of this product after the treatment process. Hence, P-H and N-O are chosen as examples of an environmentally friendly, economical, and sustainable synthesis pathway of high-performance NPs used in wastewater treatment.

Spinel Mg/Zn ferrites have also become one of the most promising adsorbents used in the treatment of wastewater due to their high levels of chemical stability, surface characteristics that can be tuned, large quantities of surface hydroxyl groups, and magnetic properties that are inherent and exploitable to separate and use after treatment as well. Mg^{2+} and Zn^{2+} are synergistically incorporated into the ferrite lattice, resulting in adsorption affinity, surface reactivity, and acidic and alkaline resistance. Recent domestic and international research has shown that $ZnFe_2O_4$ and $MgFe_2O_4$-based materials are highly effective in the removal of dyes, heavy metals and emerging contaminants, with adsorption capacities on the order of 30–50 mg g^{-1} and a high level of recycling, although the vast majority of reported methods rely on traditional chemical synthesis strategies using toxic reagents, large amounts of energy and low sustainability. Here, the originality of the current paper is that Mg-doped $ZnFe_2O_4$ nanocomposites are synthesized greenly using P-H and N-O leaf extracts as environmentally friendly reducers and stabilizers, and a comparative analysis of two biologically-derived pathways is given. Such an approach not only removes dangerous chemicals, but also grandiose invasive and conveniently located plant materials, leading to magnetically recoverable nanoadsorbents with increased adsorption and high sustainable wastewater treatment capabilities.

2. Materials and methods

2.1. Plant extract formulation

Parthenium hysterophorus plants were carefully harvested and then rinsed thoroughly to remove any soil or impurities. They were then dried at low-temperature (40–45 °C) in oven until completely dried. If using fresh material, drying can be skipped, but be aware that the extraction may yield more water content. The plant material was then crushed using a mortar and pestle or a blender until it became a fine powder. The plant powder was mixed with distilled water at a typical ratio of 1 : 10 (1 part plant material to 10 parts water). The mixture was stirred thoroughly and left for 24–48 hours at room temperature to allow for full extraction of bioactive compounds.[21]

2.2. Green synthesis of ferrites

Zinc chloride ($ZnCl_2$), iron chloride ($FeCl_2$), magnesium sulphate ($Mg(SO_4)_2$), NaOH, and HCl were used throughout the experiment; all compounds were utilized directly without further purification. The P-H and N-O plant extracts were used as reducing, capping, and stabilizing agents. Aqueous solutions (0.1 M, 50 mL) of $ZnCl_2$, (0.1 M, 50 mL) of $Mg(SO_4)_2$, and (0.2 M, 50 mL) of $FeCl_2$ were prepared in a glass beaker and agitated for 30 minutes to achieve an evenly distributed mixture with the incorporation of 50 mL of extract of P-H or N-O. Crystals of 0.01 M NaOH were added to the above solution with constant stirring while maintaining a pH of up to 10. The subsequently formed precipitates exhibited a brown hue and were filtered and desiccated in a hot oven.[22] Fig. 1 shows a schematic representation of the synthesis of ferrites.

2.3. Characterization

The morphological features and elemental distribution of the obtained sample were analyzed with the help of a scanning electron microscope (SEM, JEOL JMT 300). The crystalline structure was determined using powder X-ray diffraction (XRD, Rigaku). Functional groups and metal–metal bonding of the

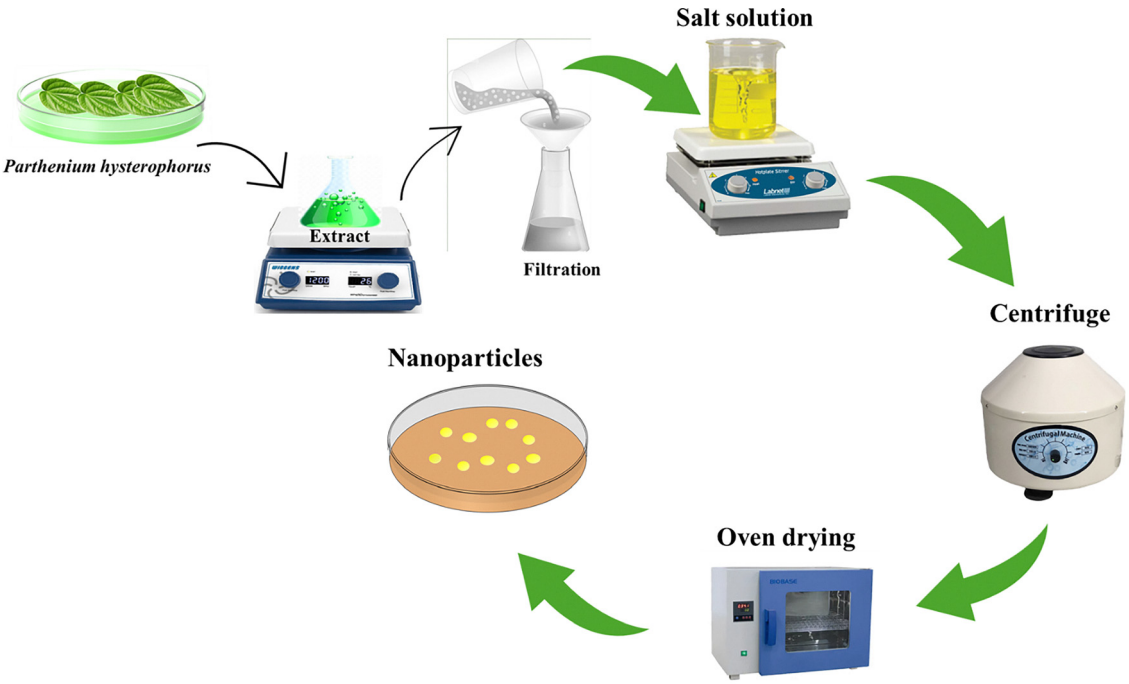

Fig. 1 Schematic representation of the synthesis of ferrites.

materials were determined by Fourier-transform infrared spectroscopy (FTIR, Bruker Tensor 27). The adsorption experiments were conducted using UV-vis spectrometer (CECIL, CE 7400).

2.4. Batch experiments

The sorption capabilities of the ferrites were compared by batch tests. By employing a traditional approach, it was possible to improve vital process variables such as pH, contact duration, initial dye concentration, sorbent dose, and temperature for the removal of dye. In an orbital shaking incubator (PA250/25H) running at 110 rpm, 50 mL conical flasks of dye solution with known pH, concentration, and sorbent dose were shaken. Except for adding sorbent, the same conditions were used for running blank solutions. 0.1 M hydrochloric acid and sodium hydroxide solutions were used to change the solution's pH. Reported values were presented as mean ± SD, and each experiment was carried out twice. The samples were removed after a certain amount of time, and centrifugation was carried out for 20 minutes at 3500 rpm. The leftover solution's concentration of dye was then evaluated using a UV-vis spectrophotometer.

Using the following relationship, the equilibrium sorption uptake, q_e (mg g^{-1}), was computed.

$$q_e = \frac{C_0 - C_e}{W} \quad (1)$$

3. Results and discussion

3.1. X-ray diffraction (XRD) analysis

The approximate position of the cations and the structural features of the magnesium zinc ferrite NPs' crystal lattice were found by XRD. The sample's diffraction sequence was found to be between 10.0° and 120.0°, falling within the 2θ range. XRD was initially used to study the phase composition and crystallinity of the synthesized samples of N-O/MgFeO. The diffraction patterns have typical peaks at 2θ values of about 30.2, 36.0, 43.3, 74.5, and 111.8 which can be indexed to the (001), (110), (111), (100), and (332) crystal planes of the cubic structure of spinel ferrite, respectively, in very good agreement with standard JCPDS data (Fig. 2).[23,24] The lack of impurity peaks is an affirmation of the successfulness of Mg/Zn ferrite phase formation through the green synthesis route. Fig. 2 highlights that the P-H/MgFeO peak with the maximum intensity lies between 35.8, 62.5, and 69.8 degrees, which can be indexed to the (110), (220), and (002) crystal planes of the cubic structure of spinel

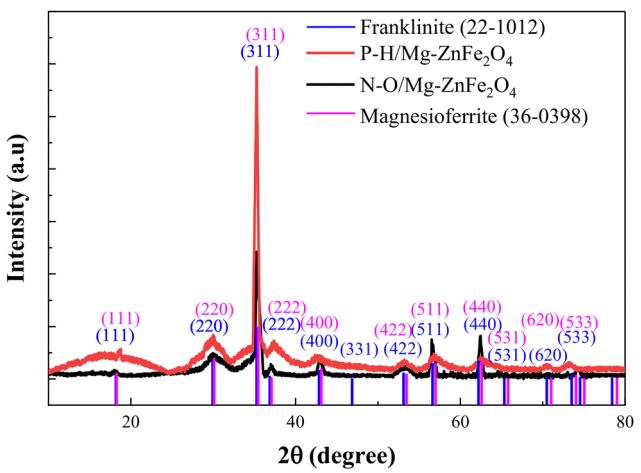

Fig. 2 XRD analysis of P-H/MgZnFe$_2$O$_4$ and N-O/MgZnFe$_2$O$_4$.

ferrite, respectively.[25] X-ray examination revealed that the magnesium zinc ferrite was single-phase and additionally showed that the spinel exhibited a cubic shape.[26]

3.2. Scanning electron microscopy (SEM)

The SEM appearance of the ferrite reveals its exterior appearance and particle size. As can be seen from the SEM portrait, ferrite has a narrow size range and a rather uniform spherical shape. Fig. 3(a–f) shows SEM microphotographs of ferrites taken using the coprecipitation process due to their magnetic properties, revealing the development of small, spherical particles reporting similar outcomes.[27,28] Due to the extensive gas release during the synthesis process, the samples' surfaces have a porous mesh-like microstructure. The surface is covered in pores of various sizes that are widely dispersed. For all samples, uniform macropores between 1–2 μm can be seen.

3.2.1. FTIR analysis. To determine the functional group responsible for the dye's adsorption on the ferrites, FTIR analysis was performed. P-H or N-O, with an iron oxide, hydroxyl functional group, was responsible for a peak between 3000 and 3500 cm^{-1} (Fig. 4(a and b)). Further peaks were detected between 1640 and 1850 cm^{-1} and between 1500 and 2000 cm^{-1}, which can be associated with nitro and carbonyl groups. The ester carbonyl compound was the cause of the peak at 1090 cm^{-1}. A broad peak between 3000 and 3500 cm^{-1} in the P-H/N-O/iron oxide specifies the existence of a hydroxyl group.[29] There is a nitro group peak at 1413, and peaks in the range of 490–660 cm^{-1} indicate the presence of halogen compounds (Fig. 4(a and b)). The peaks between 835 and 860 cm^{-1} revealed the presence of aromatic chemicals.[30] The presence of diketones was indicated by the peaks between 1535 and 1640 cm^{-1}. The differences in peak strength indicate that these functional groups, which might be phenols and alcohols found in biomolecules from leaf extracts used in the production of ferrites, are involved in the binding of color.[31] H-bonding, nitro groups, aromatic systems, phenol, ethers, and alcohols were among the other peaks whose intensities varied for ferrites. These biomolecules are obtained from plant extracts that are utilized to create adsorbents.

3.3. TGA analysis

The typical behavior of the TG curve during the heating of a ferrite sample in a thermal analyzer is shown in Fig. 5. Clearly, the change in mass of the ferrite sample occurred continuously in a certain temperature range (55–600 °C). There was a minor reduction in mass when the temperature rose to 200 °C, and then there was a sharp reduction in mass from 200–300 °C. After this, a further increase in temperature caused no change in the N-O/$MgFe_2O_4$, and it became stable, while in P-H/$MgFe_2O_4$, continued mass reduction was observed until the temperature reached 600 °C.[32]

4. Batch study optimization of significant procedure variables

4.1. Impact of pH

Both dyes and biosorbents' electrostatic attraction, ionic properties, and molecular structure are influenced by pH. As a result, it is crucial for the adsorption of dyes. The initial pH range used for the adsorption studies was 2 to 12 (Fig. 6). The influence of pH on the dye's aptitude to bind to biosorbents was investigated. Functional groups on the ferrites become ionized at pH 2, which improves the electrostatic interaction between the negatively ionized anionic dye molecules and the positively charged biosorbent surface. This is why, the highest dye adsorption was achieved at pH 2 (Fig. 6). More negatively

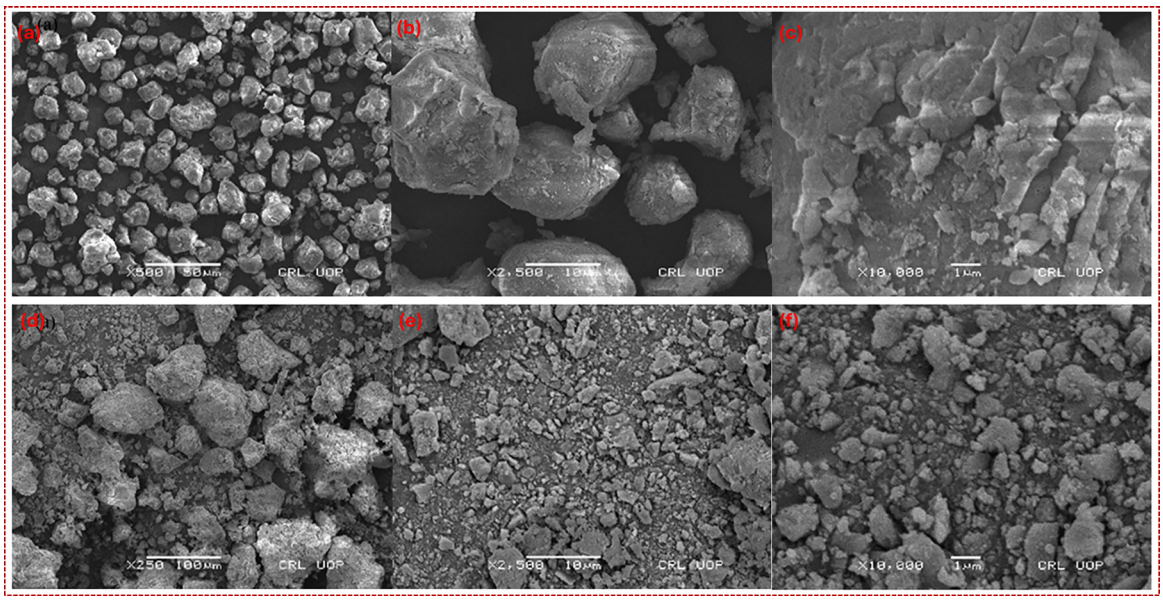

Fig. 3 (a)–(c) SEM of N-O/$MgZnFe_2O_4$ at magnification of (a) X 500, (b) X 2500 and (c) X 10 000. (d)–(f) SEM of PH/$MgZnFe_2O_4$ by zooming in at (d) X 500, (e) X 2500 and (f) X 10 000.

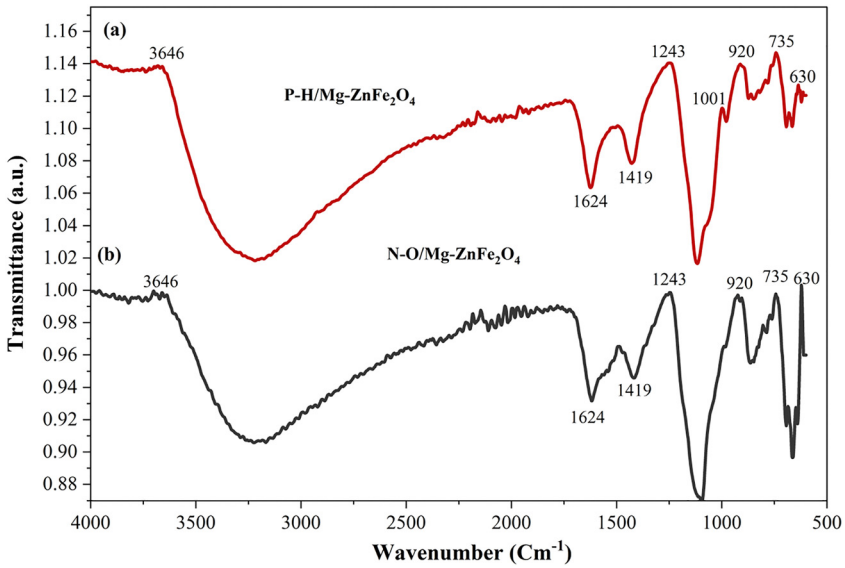

Fig. 4 FTIR analysis of (a) P-H/$MgZnFe_2O_4$ and (b) N-O/$MgZnFe_2O_4$.

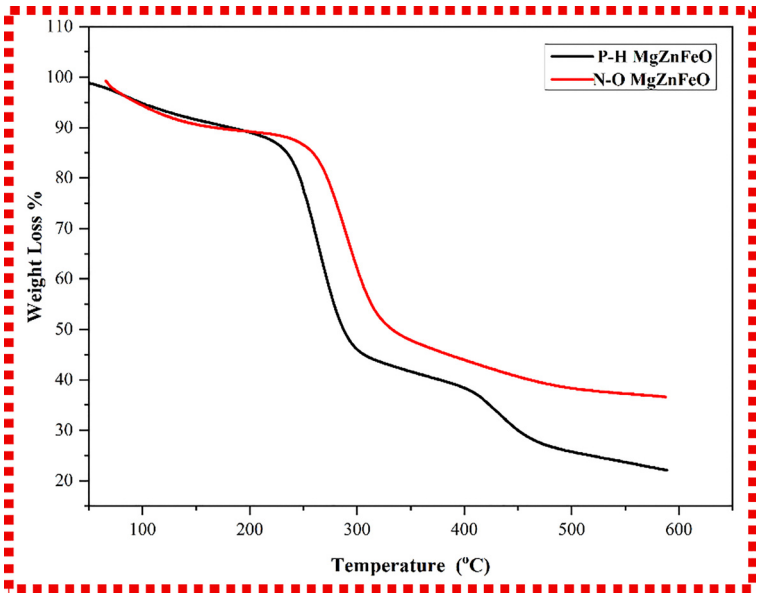

Fig. 5 TGA analysis of P-H/Mg–$ZnFe_2O_4$, and N-O/Mg–$ZnFe_2O_4$.

charged sites are present on the biosorbent, when the pH level was raised. Surplus OH^- ions interact with dye anions for sites of adsorption on the biosorbent, destabilizing anionic dyes at alkaline pH values.[33] This lowers the dye adsorption. Further research was conducted using the effective pH value (2). The sorbent solution had a 25 °C temperature, a 120-rpm shaking speed, a 0.03 g/50 mL biosorbent dose, and a 50 mg L^{-1} starting dye concentration; moreover, 0.1 M HCl or NaOH was used to change the pH of the solution.[34]

Since pH has an impact on both the solution chemistry and adsorbent surface, it is an essential factor in determining how well biosorbents work in keeping dyes out of aqueous media. The outcome of pH changes for N-O, P-H, N-O/$MgZnFe_2O_4$, and P-H/$MgZnFe_2O_4$ is shown in Fig. 6. The results indicate that pH has a significant impact on the release of dye using the nanoadsorbents N-O/$MgZnFe_2O_4$ and P-H/$MgZnFe_2O_4$. The intense sorption ability of N-O (35.93 mg g^{-1}), P-H (37.93 mg g^{-1}), N-O/$MgZnFe_2O_4$ (39.93), and P-H/Mg $ZnFe_2O_4$ (41.93) at pH 2 was recorded.[35] The decrease in adsorbent capacity at higher pH may perhaps be related to the adsorption agent's negative charge, which results in reduced adsorption. Because it improves the electrostatic contact between the dye and the nano adsorbents, the generation of H^+ ions on the biosorbent's exterior surfaces increases the rate of adsorption.[36] Also, dye adsorption studies were conducted at several pH levels.

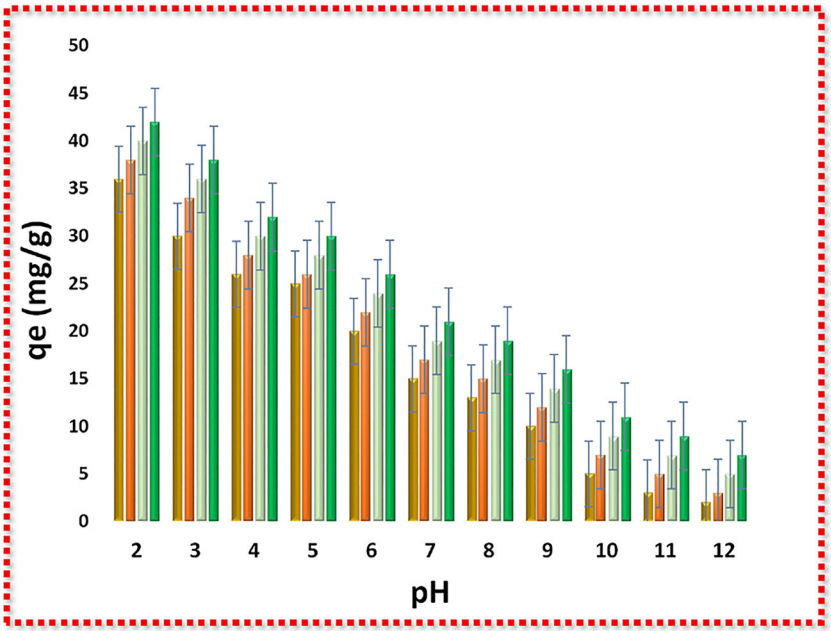

Fig. 6 Influence of pH on dye elimination employing biosorbents. Conditions: 0.03 g/50 mL biosorbent dosage, 25 °C temperature, 90 minutes' worth of contact time, and a shaking speed of 120 rpm.

4.2. Effect of adsorbent dosage

Amongst the most essential aspects of a cost-effective and effective dye adsorption process is the optimum dosage of adsorbent. The effectiveness of dye removal rises as the biosorbent dosage is increased. It might be caused by an increase in the adsorbents' active sites. The longer diffusion channel may be responsible for the smooth improvement in the discharge of the coloring material with a larger sorbent dose.[37] Adsorption of the dye rises with adsorbent dosage due to a change in sorbent and the accessibility of more surface assimilation sites. Adsorption capacity, on the other hand, decreased with increasing adsorbent amount as measured in milligrams. The overlapping or aggregation of areas of adsorption could have been correlated with it, which lessens the inclusive amount of adsorption accessible to the dye and lengthens the diffusion path.[38,39]

Adsorbent dosage is an important aspect of adsorption. This was investigated in the assortment of 0.01–0.3 at pH 2, 25 °C, and 120 rpm shaking speed. The outcomes showed that the nanoadsorbent dose had an impact on dye adsorption, with impactful adsorption capacities of N-O (52.92 mg g^{-1}), P-H (52.93 mg g^{-1}), N-O/$MgZnFe_2O_4$ (62.93 mg g^{-1}), and P-H/$MgZnFe_2O_4$ (62.93 mg g^{-1}), respectively, at a dose of 0.01 g (Fig. 7). When the doses of nanoadsorbents were increased, the sorption capacity quickly decreased. The proportion of dye exclusion was originally amplified owing to the existence of active sites, but as they were depleted.[40] The percentage of dye removal decreased, which is surface area dependent, and particle overlapping, which hinders the binding sites, was the reason for the decrease in sorption capacity at high doses. In addition, the effect of the iron oxide NPs' adsorbent dose was investigated, and it was discovered that adsorption was stronger at low adsorbent doses. Likewise, it showed that the dye adsorption tendency was consistent with what had been seen in the current experiment.[41]

4.3. Effect of contact time

The contact period between the adsorbent and dye is a requisite parameter to build an effective adsorption procedure and foretell the adsorption process mechanism. The contact duration between the adsorbent and dye is a crucial factor. The dye decrease, however, is partly ascribed to an intraparticle diffusion through the sample pores during prolonged contact times and is impacted by the distribution of pores of varying sizes throughout the entire sample matrix. The contact time, which affects the sorption process, was investigated for N-O, P-H, N-O/$MgZnFe_2O_4$, and P-H/$MgZnFe_2O_4$ at pH 2, 0.01 g dosage, 120 rpm, and 25 °C.[42] The findings are shown in Fig. 8. The data showed that adsorption was highly swift for the initial 50 minutes, then slowed and reached equilibrium after 80 minutes. The maximum adsorption capabilities were measured to be N-O (21.43 mg g^{-1}), P-H (22.83 mg g^{-1}), N-O/$MgZnFe_2O_4$ (27.43 mg g^{-1}), and P-H/$MgZnFe_2O_4$ (29.83 mg g^{-1}). The highest dye adsorption capacity was seen at 80 minutes, and this time was considered the contact time (Fig. 8). Similar results were obtained for azo dye amputation utilizing NPs composed of polypyrroles or polyanilines. The proportion of adsorption rose at first before slowing. The decrease in adsorption capacity was caused by a decrease in surface area, which also impacted the availability of active binding sites as equilibrium neared as well.[43]

Previous studies reported that the adsorption process was examined with relation to the span of contact, it was discovered

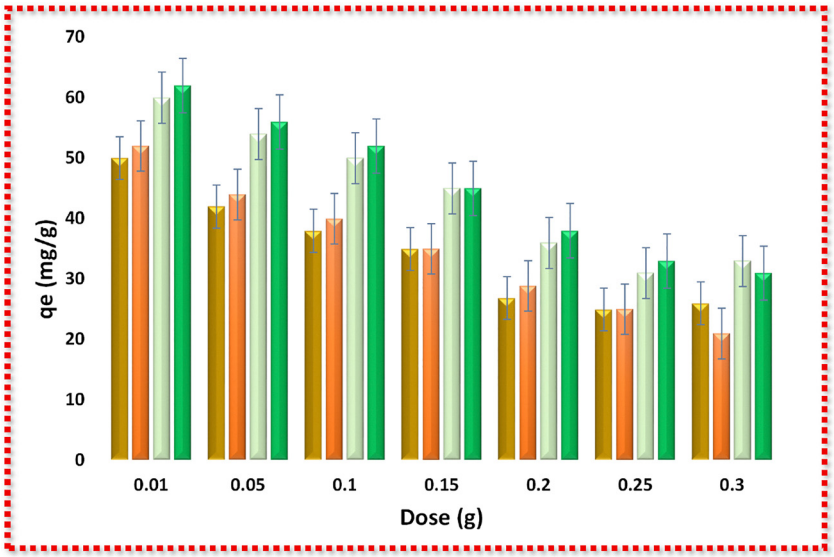

Fig. 7 Dosage effects on dye elimination utilizing biosorbents. Conditions: optimal pH 2, 25 °C temperature, 120 rpm shaking speed, and contact time 90 minutes.

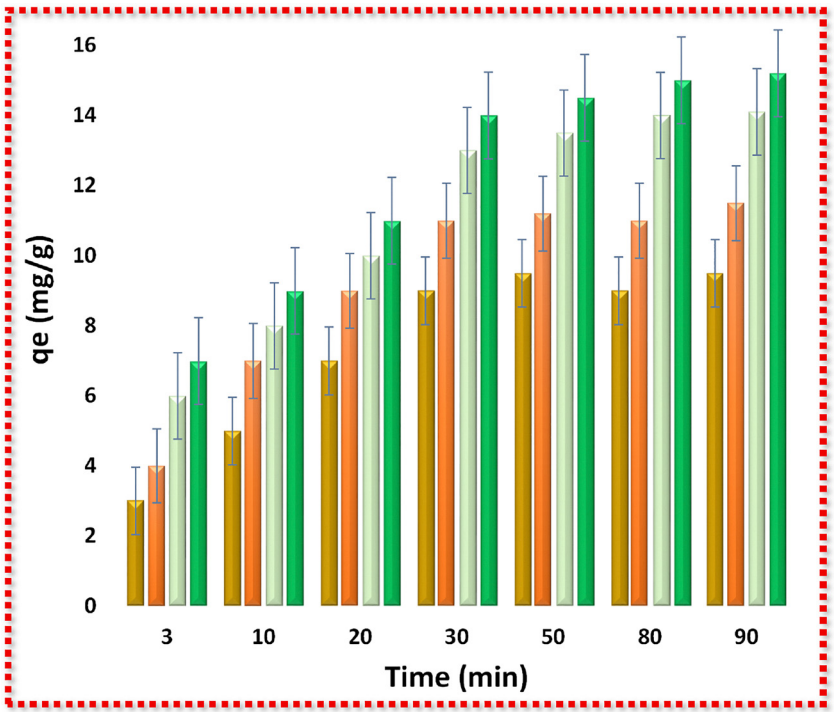

Fig. 8 Influence of contact duration on dye removal by biosorbents. Conditions: optimal pH 2, 0.01 g/50 mL biosorbent dose, 25 °C temperature, and 120 rpm shaking speed.

that, correspondingly, for iron oxide NPs, iron oxide/AgNPs, and iron oxide/AuNPs, within 30 minutes, up to 24%, 15%, and 12% dye exclusion was accomplished. The adsorption started quickly but ultimately slowed down. Compared to iron oxide NPs and iron oxide/AgNPs, which both removed 90% of the dye after 70 minutes, iron oxide/AuNPs eliminated more than 91% of the dye in 90 minutes.[44]

4.4. Effect of initial concentration of dye

The concentration of dye counts among the most decisive aspects to contemplate when creating any adsorption process. The biosorbents' ability to bind dyes was tested at various dye concentrations. As the initial dye concentration increases, the dye clearance decreases, as shown in Fig. 9. This can be explained by the fact that dye molecules clog up the adsorbent's

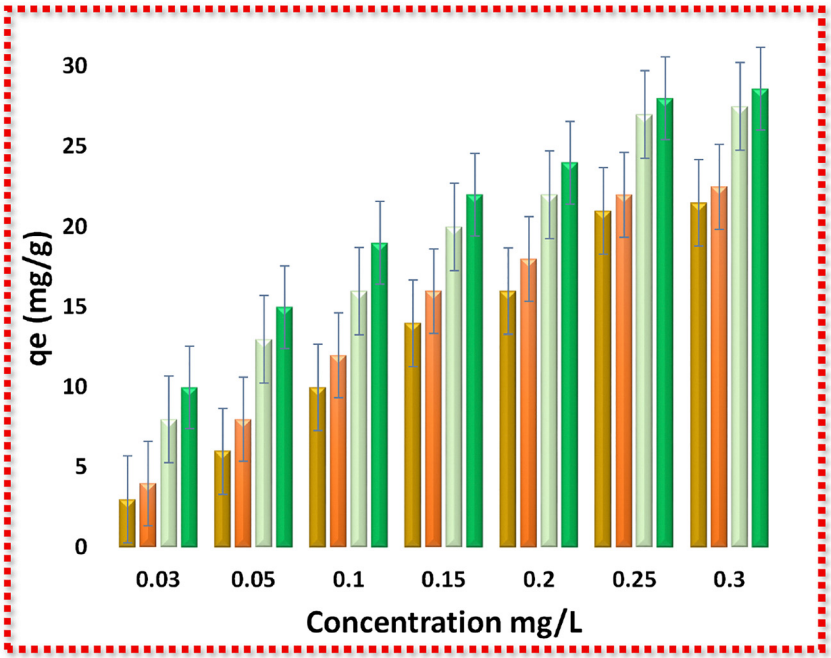

Fig. 9 Concentration's consequences for dye removal implementing biosorbents. Conditions: optimum pH 2, 0.01 g dose, 25 °C temperature, 120 rpm shaking speed, and 80 minutes contact time.

active sites, which makes it less able to bind dye solutions with higher concentrations. At a constant indefinite quantity of the biosorbents, the dye sorption capability decreases while the clearance percentage decreases.[45] At lower concentrations, the divisional adsorption is independent of the original dye concentration because there are fewer starting dye moles than there are available adsorption sites on the biosorbents.[46] The initial concentration of the dye mixture, which was considered at pH 2, 90 min of the contact period, 0.01 g/adsorbent material amount, 25 °C, and 120-rpm, also affects the sorption capacity of nanoadsorbents (Fig. 9). The adsorption effectiveness was found to be impacted by the starting dye concentration, and the three materials with the highest sorption volumes were N-O (32.89 mg g^{-1}), P-H (26.91 mg g^{-1}), N-O/$MgZnFe_2O_4$ (34.93 mg g^{-1}), and P-H/Mg–$ZnFe_2O_4$. The forces required for mass transfer between two phases, in addition to equilibrium among the solution's concentration and the adsorbent material, are provided by the dye concentration. Similarly, studies have demonstrated that the initial concentration affects dye adsorption onto composites.[47] The observations that were recorded by us are also in keeping with recent research that found that the adsorption effectiveness of biocomposites depended on the starting concentration.[48] Dye adsorption augmented when the saturation range was approached, and dye was adsorbed after the saturation limit because there were not enough active sites left. Electrostatic forces of attraction hold the dye molecules to the adsorbent surface, and dye adsorption decreases as the number of active binding sites decreases.

4.5. Effect of temperature

Temperature is a substantial component in the development of sorption systems for their applications for actual wastes, as well as a significant influence in the biosorption process of dyes, since textile manufacturers frequently release their waste at sufficiently high temperatures. The effect of various course temperatures between 30 °C and 65 °C on the biosorption ability of many chosen biosorbents for the exclusion of anionic dye from industrial wastewater was evaluated under controlled experimental working settings (as shown in Fig. 10). At temperatures ranging from 25 °C to 65 °C, the bio-sorption processes of dyes on the adsorbent agent surface were investigated; the results are displayed in Fig. 10. Temperature has an impact on the nanoadsorbents' capacity to biosorb. The dye adsorption process was endothermic, as evidenced by the fact that dye removal increased with temperature. N-O (13.2 mg g^{-1}), P-H (14.1 mg g^{-1}), N-O/$MgZnFe_2O_4$ (23.4 mg g^{-1}), and P-H/$MgZnFe_2O_4$ (25.0 mg g^{-1}) had the highest maximal sorption capabilities at 65 °C. The temperature shift was a physicochemical and endothermic process, and as the temperature rose, it effect the adsorption capacity. As the temperature rises, the adsorption capacity decreases, proving that the adsorption reaction was an exothermic one. As a result, as the temperature rises, the adsorption on the catalyst surface is reduced by the surface-assimilative interactions between the coloring material particles and the active species. Endothermic reactions produced enhanced dye adsorption because of increased ion mobility and the stability of active spots at higher temperatures.[49]

4.6. Adsorption mechanism

To gain a deeper insight into the adsorption behaviour of the developed MgFeO, it is suggested to adopt a plausible adsorption mechanism in terms of surface chemistry, structural attributes, and adsorption performance. The results of XRD

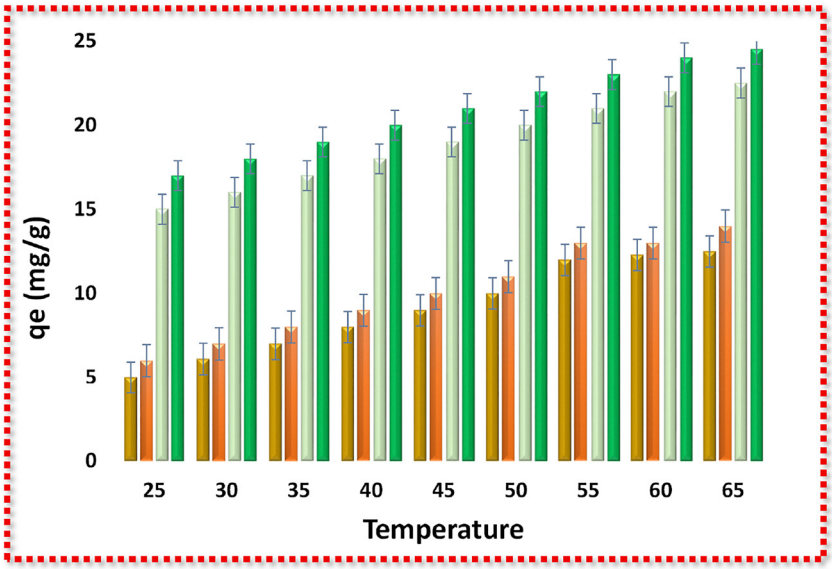

Fig. 10 Temperature's influence on dye removal *via* biosorbents. Conditions: optimal pH 2, biosorbent dose 0.01 g, 120 rpm shaking speed, and contact time 80 minutes.

and FTIR prove the availability of large quantities of surface-active sites, such as Mg–O and Fe–O functional groups, which are important in the process of pollutant uptake. In an aqueous medium, these surface sites are hydroxylated and active reactive –OH groups are formed, which can undergo a variety of interaction pathways in adsorption. The protonation or deprotonation of the surface charge of MgFeO depends on the solution pH and determines the electrostatic interactions between the adsorbent and pollutant species. Besides the electrostatic attraction, the presence of surface complexation between the metal centers (Mg^{2+}/Fe^{3+}) and functional groups of the adsorbate also contributes to the stable adsorption.[23] Moreover, hydrogen bonding and potential ion-exchange can also be involved in the general adsorption mechanism. Referring to these arguments, the following reactions are proposed and described as the mechanism of adsorption.

$$Mg–Fe–O + H_2O \rightarrow Mg–Fe–OH + H^+ \quad (R1)$$

Acidic conditions

$$Mg–Fe–OH + H^+ \rightarrow Mg–Fe–OH_2^+ \quad (R2)$$

Alkaline conditions

$$Mg–Fe–OH \rightarrow Mg–Fe–O^- + H^+ \quad (R3)$$

$$Mg–Fe–OH + Pollutant \rightarrow Mg–Fe–O–Pollutant + H^+ \quad (R4)$$

$$Pollutant + OH^- \rightarrow Pollutant\ (CO_2 + H_2O) \quad (R5)$$

5. Kinetics investigations

There should be more research into the adsorption rate in the state to develop a quick and accurate way to show how a solute sticks to an adsorbent. To test the experimental results, intra-particle diffusion, pseudo-first-order equation, and pseudo-second-order equation kinetics models were employed. Adsorption of dyes onto ferrites can be impacted by intra-particle diffusion resistance.[50,51] Kinetics is the examination of reaction rates and features that have an impact on them. Because it provides proof for the mechanics of chemical reactions, kinetics is important. Comprehending reaction fundamentals helps choose an optimal technique to initiate a reaction, accompanied by an innate scientific curiosity. Different reaction pathways can be utilized in various industrial procedures, and grasping the basics makes the alternative feasible. Chemical kinetics were performed to comprehend the activities that take place during a reaction, to pinpoint what governs its rate, and to make predictions about the composition of reaction mixtures as a function of time. The pertinency of several kinetics models, such as pseudo 1st order, pseudo 2nd order, and intra-particle diffusion, has been examined to assess the sorption investigational data of reactive methyl orange dye employing different types of biosorbents. Investigating the sorption mechanism and potential rate-controlling processes, including mass transfer and chemical reactions, was done as a result.

5.1. Pseudo-first order

Bimolecular reactions that exhibit features typical of first-order chemical reactions have been identified as pseudo-first-order reactions. This reaction takes place whenever the amount present of one of the reactive substances is maintained at a constant level or is substantially greater compared to the concentration of the other component. An example of pseudo-first-order kinetics is a crucial one. This occurs when a reaction is first order concerning two reactants but is second order overall. This kinetic system is quite prevalent at a rate = $k[A][B]$.

5.2. Pseudo-second order

Predicted on the notion that chemical sorption is the rate-limiting step, this model forecasts behavior across the full adsorption range. In this case, adsorption capacity determines the adsorption rate. The three parameter-dependent reactions are known as pseudo-second order reactions when one of the three parameters is thought to be constant.

5.3. Intraparticle diffusion

The intraparticle diffusion model (IPD) familiarized by Weber and Morris was used to analyze the kinetics of adsorption. In this study, different starting adsorption variables were used to plot the distinctive curves rooted in this model (Ri). One of the most often employed adsorption kinetic models is the intraparticle diffusion model. The application and solution of this paradigm, however, have not yet been considered. $q_t = kt^{1/2}$ and $q_t = kt^{1/2}$ are two variations of this model that have not yet been integrated, where q_t stands for adsorption capacity at time t and k is a constant, and they are model specifications. Furthermore, there is no theoretical foundation for the interpretation of this kinetic model; intraparticle diffusion dominates the adsorption; otherwise, numerous adsorption processes occur. The model interprets the mass transfer processes. The mass transfer step indicated by this model is a diffusion of the adsorbate in the apertures of the adsorbent.

The above table's R^2 values show that the intra-particle diffusion and kinetic model of pseudo-1st order do not significantly influence the sorption of the dyes by ferrites. The removal of dyes can be described as pseudo-second-order kinetics, as shown by the R^2 values for these kinetics. The results describe how several kinetic models may be used to scrutinize the tentative data on kinetic biosorption. Values of parameters for the biosorption of methyl orange dye using the N-O, P-H, N-O/$MgZnFe_2O_4$, and P-H/$MgZnFe_2O_4$ ferrites as biosorbents are shown in Table 1.

With higher correlation coefficients (R^2) in the assortment of (0.9925–0.9985) and a good degree of agreement between the estimated and experimental q_e values (mg g^{-1}), these findings exhibited that the pseudo 2nd order kinetic model could be applied to the kinetic data. The pseudo-first-order kinetic models' suitability was not significantly better on the biosorption courses of N-O, P-H, N-O/Mg–$ZnFe_2O_4$, and P-H/$MgZnFe_2O_4$, given the high degree of agreement between the estimated and experimental values, whereas the pseudo-second order kinetic model's suitability was significantly better. All used biosorbents for the removal of methyl orange showed some degree of suitability, with a lower correlation coefficient value (R^2).

Table 1 Kinetic modeling of data for the exclusion of methyl orange dye by using biosorbents

Kinetic models	N-O	P-H	N-O/Mg–$ZnFe_2O_4$	P-H/Mg–$ZnFe_2O_4$
Pseudo first order				
K_1 (L min^{-1})	0.054	0.038	0.067	0.065
q_e experimental (mg g^{-1})	33.54	43.32	123.4	122.9
q_e calculated (mg g^{-1})	52.43	69.74	45.74	45.8
R^2	0.95	0.96	0.87	0.86
Pseudo 2nd order				
K_2 (L min^{-1})	0.134	0.133	0.176	0.175
q_e experimental (mg g^{-1})	33.42	32.96	113.52	112.98
q_e calculated (mg g^{-1})	38.46	38.56	117.02	116.97
R^2	0.994	0.981	0.9992	0.993
Intraparticle diffusion				
K_{p1} (mg g^{-1} $min^{-1/2}$)	3.64	3.69	7.48	6.54
C_1	59.87	59.84	58.728	59.421
R^2	0.976	0.98	0.826	0.97

6. Biosorption isotherms

The adsorption process has drawn a lot of attention among the many techniques created in the purification and separation industries due to its affordability, user-friendliness, and environmental friendliness. The significance of the adsorption process has led to exceptional efforts throughout the years to model the adsorption isotherms. Establishing the best correlation for the equilibrium curves is crucial for an optimized design of an adsorption system. To achieve this, many isotherm equations, including the Langmuir, the Freundlich, and the Temkin adsorption isotherms, were investigated.

6.1. Langmuir biosorption isotherm

The sorption of dye on adsorbents is usually explained using the Langmuir isotherm, which has been effectively employed for a variety of sorption processes. According to the Langmuir theory, certain locations on the adsorbent surface are where sorption occurs.[52] When the adsorbate being utilized is limited to a single molecular layer, the state of equilibrium between the adsorbent system and the adsorbate is defined by the Langmuir isotherm for adsorption. The Langmuir equation can be inscribed as follows:

$$\frac{C_e}{q_e} = \frac{1}{q_m b} + \frac{C_e}{q_m} \quad (2)$$

In the above equation, q_m (mg g^{-1}) stands for maximal biosorption capacity, b (mg L^{-1}) for biosorption energy, and C_e (mg L^{-1}) for the equilibrium sorbate concentration. The fundamental property of the Langmuir isotherm is articulated by the unitless constant acknowledged as the equilibrium parameter, or R_L; R_L is defined by the equation below.

$$R_L = \frac{1}{1 + bC_0} \quad (3)$$

where C_0 is the dye's starting concentration (in mg L^{-1}).

6.2. Freundlich biosorption isotherm

The Freundlich equation indicates the possibility that the sorption heat is distributed unevenly across a heterogeneous surface.[30] The Freundlich equation can be written as follows.

$$\log q_e = \log K_F + \frac{1}{n}\log C_e \quad (4)$$

where 'n' is the adsorption intensity and K_F is a constant. The value of n allows one to calculate the biosorption's departure from linearity. The linear biosorption is represented by $n = 1$, and the favorable adsorption process is illustrated by $n > 1$. The slope and intercept of the plot between $\log q_e$ and $\log C_e$, correspondingly, were used to estimate the K_F and 'n'.

6.3. Temkin biosorption isotherm

Under the Temkin isotherm approach, the adsorption heat of all molecules falls off progressively as the adsorbent surface gets covered more until it reaches its maximum binding energy. The slope and intercept of a graph between q_e and $\ln C_e$, individually, were used to calculate the values of A and B.

$$q_e = B \ln A + B \ln C_e \quad (5)$$

6.4. Harkins–Jura biosorption isotherm

The creation of several sorbate layers on the surface of the biosorbent is said to be the outcome of the heterogeneous dispersal of minute openings, according to the Harkins–Jura biosorption isotherm. This model linear equation has the following form

$$\frac{1}{q_e^2} = \left(\frac{B}{A}\right) - \left(\frac{1}{A}\right) \log C_e \quad (6)$$

In the above equation, A = Harkins–Jura parameter and B = a constant.

The results demonstrate the multifarious character of the biosorbent particles and the formation of single and multilayer dye fragments on the exterior of the biosorbent. R^2 values of all N-O, P-H, N-O/$MgZnFe_2O_4$, and P-H/$MgZnFe_2O_4$ ferrites fall between 0.997 and 0.998. The range of R_L values from 0 to 1 showed that all biosorption processes for biosorbents were of good character. It was also determined whether the Temkin biosorption isotherm was appropriate. Because of the significant differences between the predicted and experimental q_m (mg g^{-1}) and the low values of R^2, the Harkins–Jura biosorption isotherm revealed that all of the biosorbents were the least accurate for predicting biosorption equilibrium data. Table 2 highlights the equilibrium modeling of data to remove methyl orange.

6.5. Thermodynamic studies

The most important study in thermodynamics is to determine the nature of the biosorption process. To exclude methyl orange dye utilizing different selected catalysts, the values of thermodynamic factors using the biosorption thermal records are determined.[27,53] The following equation was used to determine the values of G° for methyl orange dye at various temperatures. Different parameters of thermodynamics studies as shown in the following equation.

$$\Delta G^\circ = \Delta H^\circ - T\Delta S^\circ \quad (7)$$

$$\Delta G^\circ = -RT \ln K_d \quad (8)$$

where $K_d = q_e/C_e$ is a constant.

Table 2 Equilibrium modeling of data to remove methyl orange

Isotherm models	Methyl orange			
	N-O	P-H	N-O/$MgZnFe_2O_4$	P-H/$MgZnFe_2O_4$
Langmuir				
q_m Cal (mg g^{-1})	27.80	31.65	21.14	22.09
q_m Exp (mg g^{-1})	32.87	26.90	24.31	20.80
B	0.460	0.275	0.207	0.209
R_L	0.124	0.174	0.071	0.074
R^2	0.975	0.983	0.995	0.998
Freundlich				
q_m Cal (mg g^{-1})	87.95	108.9	2.3×10^{11}	2.5×10^{12}
K_F	8.96	4.88	2.45	2.49
N	2.96	4.87	3.44	3.47
R^2	0.932	0.96	0.94	0.98
Temkin				
q_m Cal (mg g^{-1})	679	378	351.9	352.7
A	2.84	0.86	0.31	0.39
B	7.96	5.94	10.9	11.1
R^2	0.98	0.97	0.983	0.97
Harkins–Jura				
q_m Cal (mg g^{-1})	1.79	0.79	1.45	1.46
A	56.85	45.76	97.64	98.34
B	1.96	1.096	2.18	2.21
R^2	0.86	0.965	0.981	0.971

Table 3 Methyl orange dye removal considering parameters from thermodynamics

Thermodynamic parameters	Methyl orange dye					
	298	303	308	313	318	323
N-O						
ΔG° (kJ mol^{-1})	5.99	5.95	5.28	4.98	3.99	3.87
ΔH° (kJ mol^{-1})	60.92					
ΔS° (J mol^{-1} K^{-1})	301.52					
P-H						
ΔG° (kJ mol^{-1})	8.84	7.98	7.21	6.86	4.96	3.89
ΔH° (kJ mol^{-1})	62.32					
ΔS° (J mol^{-1} K^{-1})	298.65					
N-O/$MgZnFe_2O_4$						
ΔG° (kJ mol^{-1})	6.46	5.69	4.47	3.98	2.93	1.96
ΔH° (kJ mol^{-1})	61.34					
ΔS° (J mol^{-1} K^{-1})	296.95					
P-H/$MgZnFe_2O_4$						
ΔG° (kJ mol^{-1})	6.45	5.98	4.74	3.97	2.98	1.94
ΔH° (kJ mol^{-1})	59.99					
ΔS° (J mol^{-1} K^{-1})	294.98					

The calculated thermodynamic parameters are displayed in Table 3. The presence of disorder in phases is indicated by positive S° values. The dye sorption onto the ferrite was an endothermic reaction, as evidenced by the positive H° values.

7. Conclusion and future recommendations

The present study proves the successful green synthesis of Mg/Zn ferrites using plant extracts of P-H and N-O as reducing and stabilizing agents. The ferrites had a high adsorption performance for textile dyes, where the efficiency was significantly affected by pH, adsorbent dosage, contact time, temperature, and initial concentration of dye. Kinetic experiments

showed that dye adsorption mainly obeyed the pseudo-second-order model along with intraparticle diffusion, whereas isotherm studies showed that they fit well with the Langmuir, and Temkin models. Thermodynamic parameters were used to confirm the spontaneity and feasibility of the adsorption process. In addition, the effects of surfactants and detergents, which are prevalent as components of textile wastewaters, brought out the complexity of the real wastewater interactions. The study shows that Mg–$ZnFe_2O_4$ nanocomposites synthesized greenly have a strong adsorption behavior as compared to plant materials. The P-H/Mg–$ZnFe_2O_4$ nanocomposite had the largest adsorption capacity of about 42 mg g^{-1} in acidic conditions (pH 2), and the equilibrium was reached within 80 minutes, The highest adsorption capacities were achieved for N-O (52.92 mg g^{-1}), P-H (52.93 mg g^{-1}), N-O/$MgZnFe_2O_4$ (62.93 mg g^{-1}), and P-H/$MgZnFe_2O_4$ (62.93 mg g^{-1}), respectively. Which proves that the adsorbent is stable and can be successfully used in wastewater treatment.

Overall, the results highlight the potential of the sustainably synthesized Mg/Zn ferrites as efficient and environmentally friendly adsorbents for textile dye removal. Despite all these promising results, more effort is needed to push these materials towards real application. Future work should be aimed at studying performance in pilot-scale or continuous flow studies to assess performance under actual wastewater conditions. Investigating the regeneration capacity and long-term stability of the ferrites will be fundamental to the evaluation of the operational feasibility. In addition, further research into surface modification, magnetic recovery optimization, and performance studies in complex wastewater matrices can further enhance the adsorption efficiency and selectivity. Moreover, advanced modelling techniques such as ANN, RSM, or DFT can potentially give more mechanistic information about adsorption behaviour. Finally, comprehensive environmental risk assessments, life cycle analysis, and cost evaluations are recommended in support of the large-scale introduction of these green-synthesized ferrites in industrial wastewater treatment systems.

Conflicts of interest

There are no conflicts to declare.

Data availability

Data will be provided upon request.

References

1 A. Dinar, Challenges to water resource management: The role of economic and modeling approaches, *Water*, 2024, **16**(4), 610.
2 Z. Zhang, *et al.*, Facile hydrothermal synthesis of CuO–Cu_2O/GO nanocomposites for the photocatalytic degradation of organic dye and tetracycline pollutants, *New J. Chem.*, 2020, **44**(16), 6420–6427.
3 S. Alam, *et al.*, Preparation, Characterization and Removal of Acid Blue 129 and Erioglaucine Dyes from Aqueous Solution by Corn Cob Based Activated Carbon, *Bull. Environ. Contam. Toxicol.*, 2025, **115**(1), 4.
4 M. T. Mosisa, *et al.*, A novel V/S co-doped BiOBr catalyst for high-efficiency catalytic reduction of toxic organic and hexavalent chromium pollutants under dark, *J. Environ. Chem. Eng.*, 2024, 112111.
5 D. Van Thuan, *et al.*, Photodegradation of hazardous organic pollutants using titanium oxides-based photocatalytic: A review, *Environ. Res.*, 2023, 116000.
6 S. Dutta, *et al.*, Contamination of textile dyes in aquatic environment: Adverse impacts on aquatic ecosystem and human health, and its management using bioremediation, *J. Environ. Manage.*, 2024, **353**, 120103.
7 M. Ateia, H. Wei and S. Andreescu, Sensors for emerging water contaminants: overcoming roadblocks to innovation, *Environ. Sci. Technol.*, 2024, **58**(6), 2636–2651.
8 C. V. Reddy, *et al.*, Novel g-C3N4/BiVO4 heterostructured nanohybrids for high efficiency photocatalytic degradation of toxic chemical pollutants, *Chemosphere*, 2023, **322**, 138146.
9 F. Saadat, *et al.*, Progress in zeolite–water adsorption technologies for energy-efficient utilization, *Energy*, 2024, **308**, 133001.
10 Y. Wang, *et al.*, Research status, trends, and mechanisms of biochar adsorption for wastewater treatment: a scientometric review, *Environ. Sci. Eur.*, 2024, **36**(1), 25.
11 M. Rani, Sunlight-induced photocatalytic degradation of organic pollutants by biosynthesized hetrometallic oxides nanoparticles, *Environ. Sci. Pollut. Res.*, 2021, **28**(43), 61760–61780.
12 N. El Messaoudi, *et al.*, Green synthesis of CuFe2O4 nanoparticles from bioresource extracts and their applications in different areas: a review, *Biomass Convers. Biorefin.*, 2025, **15**(1), 99–120.
13 Z. A. Al-Ahmed, *et al.*, Recoverable palladium–gold nanocomposite based on microcrystalline cellulose for sonocatalytic degradation of pharmaceutical pollutants, *Mater. Chem. Phys.*, 2023, **296**, 127219.
14 R. Kavitha, *et al.*, Enhanced visible light-driven photocatalytic activity of green synthesized cobalt ferrite nanoparticles, *Ceram. Int.*, 2024, **50**(3), 4861–4874.
15 K. Kannan, *et al.*, Facile synthesis of novel ZnO-MgO nanohybrids and its photocatalytic degradation of toxic pollutants, *Desalin. Water Treat.*, 2024, **317**, 100125.
16 M. A. Tiawoun, *et al.*, Ecological traits and socio-economic impacts of the alien invader weed Parthenium hysterophorus L. in South Africa's rangeland ecosystems: A review, *Diversity*, 2024, **16**(4), 205.
17 S. H. Hashemi and M. Kaykhaii, Azo dyes: sources, occurrence, toxicity, sampling, analysis, and their removal methods, in *Emerging freshwater pollutants*, 2022, Elsevier, pp. 267–287.
18 A. Pandey, S. Usmani, M. Ahmad, S. Khatoon, S. Wahab and O. Prakash, *Curr. Nutr. Food Sci.*, 2024, **20**(5), 570-–585.

19 K. Chaudhary, V. B. Kushwaha and S. K. Srivastav, A review: nerium indicum or nerium oleander and its toxicity in vertebrates, *system*, 2024, **4**, 5.
20 A. Javdani-Mallak and I. Salahshoori, Environmental pollutants and exosomes: A new paradigm in environmental health and disease, *Sci. Total Environ*, 2024, 171774.
21 M. Pirsaheb, *et al.*, Green synthesis of nanomaterials by using plant extracts as reducing and capping agents, *Environ. Sci. Pollut. Res.*, 2024, **31**(17), 24768–24787.
22 G. A. Naikoo, *et al.*, Bioinspired and green synthesis of nanoparticles from plant extracts with antiviral and antimicrobial properties: A critical review, *J. Saudi Chem. Soc.*, 2021, **25**(9), 101304.
23 S. I. Siddiqui and S. A. Chaudhry, Nigella sativa plant based nanocomposite-MnFe2O4/BC: An antibacterial material for water purification, *J. Cleaner Prod.*, 2018, **200**, 996–1008.
24 A. Sharma, *et al.*, Sustainable and efficient removal of cationic and neutral dyes from aqueous solution using nano-engineered CuFe2O4/Peanut shell magnetic composite, *Clean Technol. Environ. Policy*, 2024, **26**(11), 3921–3935.
25 B. Fatima, *et al.*, Facile green synthesis of ZnO–CdWO4 nanoparticles and their potential as adsorbents to remove organic dye, *Environ. Pollut.*, 2021, **271**, 116401.
26 S. Kushwah, *et al.*, Understanding switching intentions towards renewable energy technologies using push-pull-mooring framework, *J. Cleaner Prod.*, 2024, **465**, 142656.
27 M. A. Darwish, *et al.*, Impact of the Mg/Zn ratio on features of structural and magnetic properties in A-site stoichiometric nanosized spinel ferrites, *J. Alloys Compd.*, 2023, **968**, 172278.
28 R. Jasrotia, *et al.*, Photocatalytic dye degradation efficiency and reusability of Cu-substituted Zn-Mg spinel nanoferrites for wastewater remediation, *J. Water Process Eng.*, 2022, **48**, 102865.
29 R. Jasrotia, *et al.*, Photocatalytic degradation of malachite green pollutant using novel dysprosium modified Zn–Mg photocatalysts for wastewater remediation, *Ceram. Int.*, 2022, **48**(19), 29111–29120.
30 S. Kumari, *et al.*, Retrievable nano-sized Co–Mg–Zn ferrite as an active photocatalyst and adsorbent for removing organic and biological contaminants for water purification, *Ceram. Int.*, 2024, **50**(2), 3210–3221.
31 P. Dhiman, *et al.*, Co doped Mg–Zn spinel nano-ferrites as a sustainable magnetic nano-photo-catalyst with reduced recombination for photo degradation of crystal violet, *J. Inorg. Organomet. Polym. Mater.*, 2023, **33**(9), 2776–2789.
32 S. Kumari, *et al.*, Nano Ca–Mg–Zn ferrites as tuneable photocatalyst for UV light-induced degradation of rhodamine B dye and antimicrobial behavior for water purification, *Ceram. Int.*, 2023, **49**(8), 12469–12480.
33 N. Basfer, S. Mansour and F. Al-Hazmi, Tailored dielectric, optical properties and photocatalytic performance of Mg–Zn nanoferrites by Cu2+ substitution, *J. Mater. Sci.: Mater. Electron.*, 2020, **31**(19), 16160–16177.
34 K. H. Hamad, *et al.*, Nylon fiber waste as a prominent adsorbent for Congo red dye removal, *Sci. Rep.*, 2024, **14**(1), 1088.
35 A. G. Meskel, *et al.*, Malachite green and methylene blue dye removal using modified bagasse fly ash: Adsorption optimization studies, *Environ. Challenges*, 2024, **14**, 100829.
36 K. Mensah, *et al.*, Dye removal using novel adsorbents synthesized from plastic waste and eggshell: mechanism, isotherms, kinetics, thermodynamics, regeneration, and water matrices, *Biomass Convers. Biorefin.*, 2024, **14**(12), 12945–12960.
37 Y. Özüdoğru, S. Gönülaçar and E. Yüz, Adsorption of Dyes Using From Blue Crab Shells, 2024.
38 A. Pourabadeh, *et al.*, The optimisation of operating parameters of dye removal: application of designs of experiments, *Int. J. Environ. Anal. Chem.*, 2021, **101**(9), 1320–1329.
39 S. Mansour, *et al.*, Enhanced magnetic, dielectric properties and photocatalytic activity of doped Mg–Zn ferrite nanoparticles by virtue of Sm3+ role, *J. Alloys Compd.*, 2021, **856**, 157437.
40 S. Noreen, *et al.*, Chitosan, starch, polyaniline and polypyrrole biocomposite with sugarcane bagasse for the efficient removal of Acid Black dye, *Int. J. Biol. Macromol.*, 2020, **147**, 439–452.
41 S. M. H. Asl, *et al.*, Synthesis of hydrous iron oxide/aluminum hydroxide composite loaded on coal fly ash as an effective mesoporous and low-cost sorbent for Cr (VI) sorption: fuzzy logic modeling, *Process Saf. Environ. Prot.*, 2017, **107**, 153–167.
42 S. Kour, *et al.*, Improving photocatalytic efficiency of MnFe2O4 ferrites via doping with Zn2+/La3+ ions: photocatalytic dye degradation for water remediation, *Environ. Sci. Pollut. Res.*, 2023, **30**(28), 71527–71542.
43 R. Hassan and I. Zahoor, Strategies and Technologies for Emerging Contaminants, *Int. J. Chem. Biochem. Sci.*, 2024, **25**(16), 211–228.
44 R. Batool and M. Alam, Removal of microplastics and nanoplastics from water: A review, *Int. J. Chem. Biochem. Sci.*, 2024, **25**, 193–207.
45 S. Sudan, A. Khajuria and J. Kaushal, Adsorption potential of pristine biochar synthesized from rice husk waste for the removal of Eriochrome black azo dye, *Mater. Today: Proc.*, 2023, DOI: 10.1016/j.matpr.2023.01.258.
46 N. Kumar, A. Pandey and Y. C. Sharma, A review on sustainable mesoporous activated carbon as adsorbent for efficient removal of hazardous dyes from industrial wastewater, *J. Water Process Eng.*, 2023, **54**, 104054.
47 M. Bellaj, *et al.*, Cationic and anionic dyes adsorption from wastewater by clay-chitosan composite: an integrated experimental and modeling study, *Chem. Eng. Sci.*, 2024, **285**, 119615.
48 C. E. de Farias Silva, *et al.*, Basic-dye adsorption in albedo residue: Effect of pH, contact time, temperature, dye concentration, biomass dosage, rotation and ionic strength, *J. King Saud Univ., Eng. Sci.*, 2020, **32**(6), 351–359.
49 F. H. Mustafa, *et al.*, Cost-effective removal of toxic methylene blue dye from textile effluents by new integrated crosslinked chitosan/aspartic acid hydrogels, *Int. J. Biol. Macromol.*, 2023, **248**, 125986.

50 M. A. El-Nemr, *et al.*, Isotherm and kinetic studies of acid yellow 11 dye adsorption from wastewater using Pisum Sativum peels microporous activated carbon, *Sci. Rep.*, 2023, **13**(1), 4268.
51 M. Loutfi, *et al.*, Adsorption of methylene blue dye from aqueous solutions onto natural clay: Equilibrium and kinetic studies, *Mater. Today: Proc.*, 2023, **72**, 3638–3643.
52 M. G. Fadl, Prediction of heavy metal biosorption mechanism through studying isotherm kinetic equations, *Sci. Rep.*, 2023, **13**(1), 1576.
53 G. Petroli, *et al.*, Application of artificial neural networks and Langmuir and Freundlich isotherm models to the removal of textile dye using biosorbents: A comparative study among methodologies, *Can. J. Chem. Eng.*, 2025, **103**(3), 1169–1182.